

PAPER • OPEN ACCESS

## Self-similar cuspidal formation by runaway thermocapillary forces in thin liquid films

To cite this article: Chengzhe Zhou and Sandra M Troian 2019 *New J. Phys.* **21** 013018

View the [article online](#) for updates and enhancements.



**IOP** | ebooks™

Bringing you innovative digital publishing with leading voices to create your essential collection of books in STEM research.

Start exploring the collection - download the first chapter of every title for free.



## PAPER

**Self-similar cuspidal formation by runaway thermocapillary forces in thin liquid films**

## OPEN ACCESS

## RECEIVED

26 July 2018

## REVISED

26 November 2018

## ACCEPTED FOR PUBLICATION

30 November 2018

## PUBLISHED

18 January 2019

Original content from this work may be used under the terms of the [Creative Commons Attribution 3.0 licence](https://creativecommons.org/licenses/by/4.0/).

Any further distribution of this work must maintain attribution to the author(s) and the title of the work, journal citation and DOI.

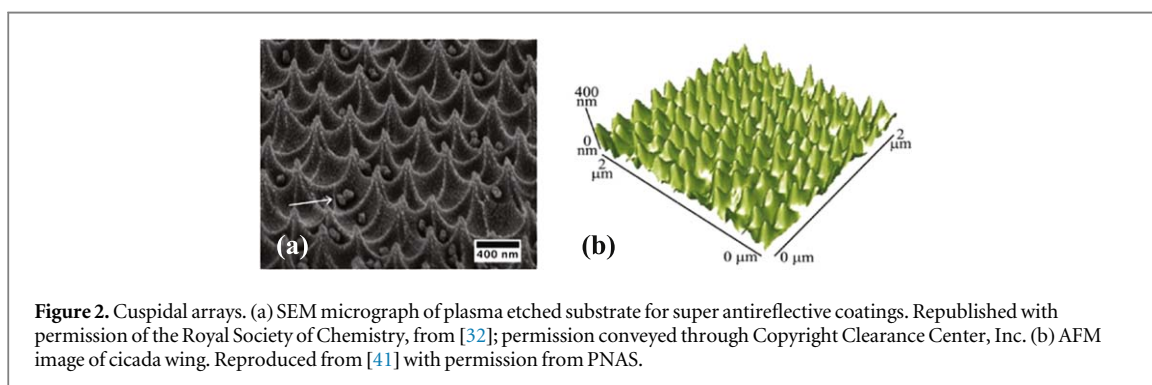
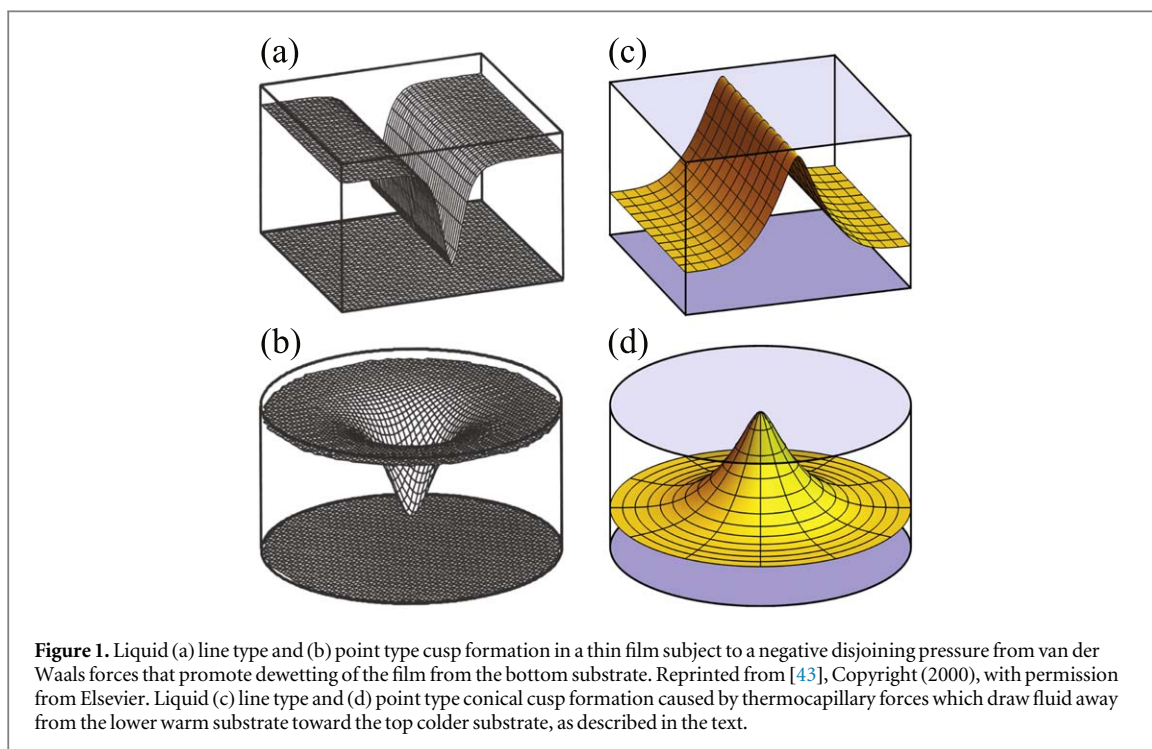
Chengzhe Zhou<sup>1</sup> and Sandra M Troian<sup>2</sup><sup>1</sup> California Institute of Technology, 1200 E. California Blvd, Physics, MC 103-33, Pasadena, CA 91125, United States of America<sup>2</sup> California Institute of Technology, 1200 E. California Blvd., Applied Physics, MC 128-95, Pasadena, CA 91125, United States of AmericaE-mail: [stroian@caltech.edu](mailto:stroian@caltech.edu)**Keywords:** thermocapillary, thin film equation, free surface cusps, self-similarity, driven singularities, runaway process, blowupSupplementary material for this article is available [online](#)**Abstract**

Many physical systems give rise to dynamical behavior leading to cuspidal shapes which represent a singularity of the governing equation. The cusp tip often exhibits self-similarity as well, indicative of scaling symmetry invariant in time up to a change of scale. Cuspidal shapes even occur in liquid systems when the driving force for fluid elongation is sufficiently strong to overcome leveling by capillarity. In almost all cases reported in the literature, however, the moving interface is assumed to be *shear-free* and the operable forces orient exclusively in the direction normal to the advancing boundary. Here we focus on a system in which a slender liquid film is exposed to large thermocapillary stresses, a system previously shown to undergo a linear instability resembling microlens arrays. We demonstrate by analytic and numerical means how in the nonlinear regime runaway thermocapillary forces induce cuspidal formations terminated by a conical tip whose slope is given by an analytic relation. On a fundamental level, this finding broadens our understanding of known categories of flows that can generate cuspidal forms. More practically, the system examined here introduces a potentially novel lithographic method for one-step non-contact fabrication of cuspidal microarrays.

**1. Cusp formation in physical systems**

Despite that capillary forces always act to repress regions of high curvature, nature nonetheless finds clever ways of forming and sustaining cusps in many physical systems. In fact, cusps are rather ubiquitous and occur in such diverse phenomena as thermal grooving at grain boundaries [1], surface diffusion and pinchoff in annealed or sintered systems [2], complex plasma formations [3], wavefront propagation in systems described by the linear [4] or nonlinear Schrödinger equation [5], critically charged droplets [6], microbranching instabilities in fast moving cracks [7], line attractor states in neural computation models [8], evaporative dryout in liquid films [9] and many more. A recent delightful book by J Eggers [10] describes as well the complex dynamics governing cusp formation in many liquid systems including thread and droplet breakup, Hele-Shaw sink flow, and thin film rupture caused by a negative disjoining pressure [2, 11, 12]. The latter system sketched in figures 1(a) and (b) shows that the receding air/liquid interface traces a cusp.

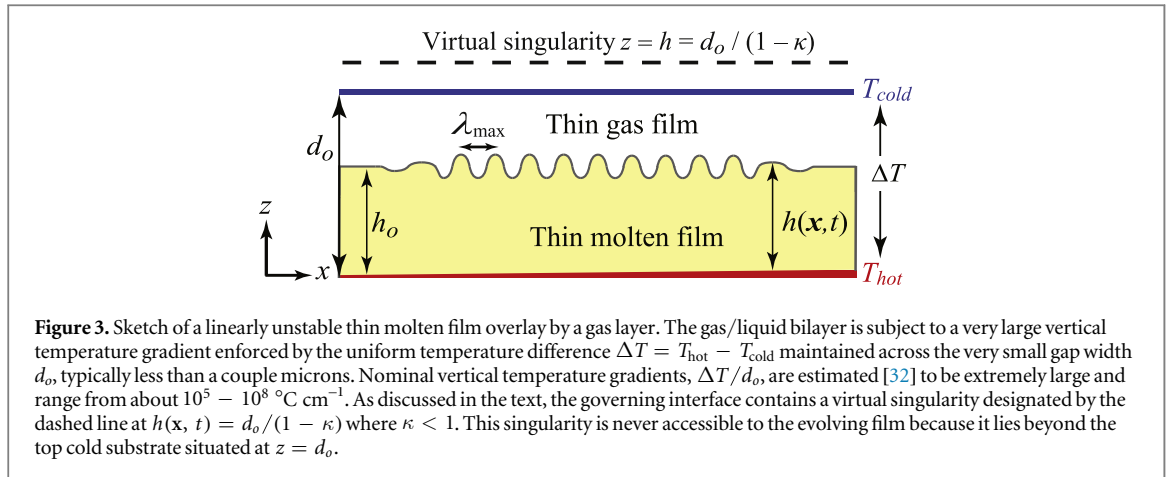
In these and other systems [14–18], the apical region of the evolving cusp exhibits self-similar behavior characterized by universal exponents, some of which have been confirmed experimentally [19–23]. The resulting power laws stem from scaling symmetries that are invariant in time up to a change of scale. In almost all cases reported in the literature, however, the moving interface is assumed to be *shear-free* and the operable surface forces orient exclusively in the direction normal to the advancing boundary. The interface therefore experiences no shear force and therefore plays no active role in corralling fluid into a sharpened tip. Krechetnikov has recently conducted elegant analyses of chemically driven tip streaming emanating from conical singularities in self-driven Marangoni systems; however, those studies have had to assume steady state (i.e. time independent) flows since the dynamics of cusp formation there remains an unsolved problem [24, 25].



To explore further the possibility of cuspidal formation driven by shear forces at a free interface, we here focus on nanoscale liquid films confined by a geometry designed to elicit self-reinforcing thermocapillary stresses at the air/liquid interface. We analyze the dynamics by which the ensuing self-similar process gives rise to fluid elongations resembling cuspidal shapes whose conical tips promote self-focusing. Shown in figures 1(c) and (d) are examples of thermocapillary driven line and point cuspidal formations caused by runaway thermocapillary forces. While figures 1(a) and (b) depict cusp formation arising from forces exclusively oriented normal to the free interface (disjoining pressure counterbalanced by capillary pressure), figures 1(c) and (d) depict formation of cuspidal shapes from thermocapillary (shear) forces which orient parallel to the moving interface. An additional challenging feature of the thermocapillary problem is that the apical region exhibits multiscale dynamics which considerably complicates the stability analysis.

Aside from such fundamental considerations, there is a practical motivation for this study as well. We are interested in exploring thermocapillary based techniques for patterning nanoscale films which can be rapidly solidified *in situ*. The system geometry examined in this work offers a potentially novel lithographic method for one-step non-contact fabrication of cuspidal microarrays. This development can facilitate design and manufacture of specialty microarrays such as biomimetic cuspidal substrates. Two recent important examples of such desirable substrates include infrared (IR) antireflective moth eye surfaces patterned with quintic cusps for eliminating Fresnel reflections in the mid-IR [26–28] as in figure 2(a), and superhydrophobic, self-cleaning antimicrobial surfaces mimicking the surface of a cicada wing [29] as in figure 2(b). Such substrates can likely be architected using thermocapillary forces to pattern thin films in which form follows function i.e. imprinted cuspidal shapes relating directly to their intended function.

Our group has previously demonstrated experimentally how large patterned thermocapillary forces can be used to sculpt nanofilms into liquid microlens arrays, which are then solidified rapidly *in situ* [30]. The resulting



ultra-smooth surfaces are ideally suited to micro-optical applications such as beam shaping. The analysis presented in this work suggests that if the microlens configurations are allowed to evolve further in time before solidification is imposed, the system will transition to a microcuspidal array. The local analysis presented in this work indicates how initial protrusions of any sort, whether triggered by the linear instability [31, 32] or triggered by large amplitude perturbations [30, 33], are expected to evolve into individual or array-like cuspidal patterns.

The outline of this work is as follows. In section 2 we present the evolution equation for an ultrathin Newtonian liquid layer subject to very large thermocapillary forces induced by thermal conduction across a slender quiescent gas film. Nominal estimates [32] extracted from experiment for the spanwise temperature gradient across the gas/liquid bilayer reveal values in the range  $10^5 - 10^8 \text{ }^\circ\text{C cm}^{-1}$ . This slender geometry is known to give rise to an initial linear instability [31, 32] which generates spontaneous periodic arrays of slender domes. The array pitch, given by the wavelength characterizing the fastest growing mode is subsequently used to rescale the original equation. Further rescaling to parameter-free dimensionless form yields an equation belonging to the general class of gradient flows. In section 3, it is shown that this evolution equation does not support stable stationary states because the dynamics incurred by the confined geometry involve runaway thermocapillary forces whereby the nanofilm can reduce its free energy by advancing ever closer to the top colder substrate. In section 4, 2D and 3D numerical solutions of the nonlinear interface equation reveal formation of a stable cuspidal shape which terminates in a cone with a rounded tip that undergoes continuous sharpening. The numerical simulations reveal the self-similar process underlying the power law growth behavior characterizing the tip speed and tip curvature. In section 5 we present an asymptotic analysis of the conical region which reveals the presence of a stable fundamental mode acting as an attractor state. Various measures characterizing this fundamental mode are shown to be in excellent quantitative agreement with the numerical simulations. The asymptotic analysis also provides an analytic relation for the slope of the conical tip which should prove useful in designing arrays with specific tip textures. In section 6, we conclude with some final thoughts on how these findings may help advance a novel lithographic method for fabrication of specialty cuspidal microarrays.

## 2. Long wavelength model for growth of protrusions by runaway thermocapillary forces

A theoretical model has previously been derived [31, 32] to describe the evolution and stability of a confined slender gas layer overlaying a nanoscale molten film as sketched in figure 3. The molten nanofilm of initial uniform or average thickness  $h_o$  is confined to a very narrow gap width  $d_o$  by two impenetrable solid substrates maintained at a uniform temperature difference  $\Delta T = T_{\text{hot}} - T_{\text{cold}} > 0$ . The nanofilm is assumed to comprise a single-component, non-volatile, incompressible liquid. The model is based on a long wavelength approximation (also called the lubrication or slender gap limit) for which the thickness of the molten film is much smaller than any characteristic lateral scale  $L$  such that  $\epsilon^2 = (h_o/L)^2 < (d_o/L)^2 \ll 1$ , inertial forces are negligible such that  $\epsilon Re \ll 1$  where  $Re$  is the Reynolds number, and thermal conduction is the dominant mode of heat transfer such that  $\epsilon RePr \ll 1$  where  $Pr$  is the Prandtl number. Estimates [32] based on experimental values have shown that hydrostatic forces are much smaller than viscous forces by at least order  $10^{-7}$  (quantified by the ratio of Bond number to capillary number) and therefore gravitational effects are also negligible. The viscosity of the film  $\mu = \mu(T_{\text{hot}})$  is also assumed relatively constant given the ultrasmall gap dimension  $d_o$ . The model also disallows any contact with the bottom or top substrate such that  $0 < h(\mathbf{x}, t) < d_o$  where  $\mathbf{x} = (x, y)$ . Since for single component fluids the variation in surface tension  $\gamma$  with temperature  $T$  given by  $d\gamma/dT$  is a negative quantity, any fluctuation giving rise to a local protrusion generates a local segment of the interface with

relatively cooler surface temperature and therefore higher surface tension. Such variations in surface temperature generate thermocapillary stresses  $\nabla_{\parallel}\gamma = (d\gamma/dT)\nabla_{\parallel}T$ , which act to pull liquid from warmer to cooler regions of the film. Within the long wavelength approximation, the operator  $\nabla_{\parallel}$  denoting the surface gradient simply reduces to  $(\partial/\partial x, \partial/\partial y)$ . The dominant shear stresses caused by thermocapillarity are therefore oriented in-plane and give rise to large lateral fluxes that push liquid into protruding regions of the film, which grow further in height and become cooler in temperature, thereby establishing a feedback mechanism.

In the long wavelength limit, the corresponding energy equation describing heat transfer across the gas/liquid bilayer reduces simply to the 1D Laplace equation  $d^2T/dz^2 = 0$  which is easily solved to give the temperature distribution along the liquid interface  $z = h(\mathbf{x}, t)$ :

$$T[h(\mathbf{x}, t)] = T_{\text{cold}} + \Delta T \frac{d_o - h(\mathbf{x}, t)}{d_o + (\kappa - 1)h(\mathbf{x}, t)}. \quad (1)$$

The material parameter  $\kappa$  denotes the ratio of gas to liquid thermal conductivity evaluated at the temperatures of the respective adjacent substrates. Since the gas layer is always more thermally insulating than the liquid layer, the ratio  $\kappa$  is restricted to the range  $0 < \kappa < 1$ . Depending on the materials of choice, however, the magnitude of  $\kappa$  can range anywhere from about 1/4 or higher for molten polymer films overlay by an air film [32] to  $10^{-4}$  or smaller for liquid metal films [34] overlay by a xenon gas layer [35]. The confined geometry therefore generates self-reinforcing runaway thermocapillary stresses, which promote growth of elongations toward the colder substrate. This process is mitigated only by capillary forces which tend to suppress regions of high curvature. The system described is known to undergo a linear instability [31, 32] which occurs irrespective of the magnitude of  $\Delta T$ . At early times, infinitesimal disturbances generate periodic undulations in film thickness which undergo exponential growth. The wavelength of the fastest growing mode is given by

$$\lambda_{\text{max}} = 2\pi h_o \left( \frac{4\gamma_o h_o}{3\kappa d_o \gamma_T \Delta T} \right)^{1/2} \left( \frac{d_o}{h_o} + \kappa - 1 \right), \quad (2)$$

where  $\gamma_o = \gamma(T_{\text{hot}})$  and  $\gamma_T = |d\gamma/dT|_{T_{\text{hot}}}$ . All else equal, a larger difference in temperature  $\Delta T$  causes undulations of smaller wavelength. Recent [36–38] and ongoing experiments to confirm the mechanism leading to instability so far indicate good agreement with predictions for the fastest growing mode and its growth rate. In what follows,  $\lambda_{\text{max}}$  is selected as the characteristic lateral scale  $L$  used to non-dimensionalize lateral scales in the governing equation of motion.

The dimensionless evolution equation describing the long wavelength thermocapillary model is given by

$$\frac{\partial \widehat{H}}{\partial \widehat{\tau}} + \widehat{\nabla}_{\parallel} \cdot \left\{ \frac{\widehat{H}^3}{3\widehat{C}\widehat{a}} \widehat{\nabla}_{\parallel} \widehat{\nabla}_{\parallel}^2 \widehat{H} + \frac{\kappa \widehat{D} \widehat{M}\widehat{a} \widehat{H}^2}{2[\widehat{D} + (\kappa - 1)\widehat{H}]^2} \widehat{\nabla}_{\parallel} \widehat{H} \right\} = 0. \quad (3)$$

Here  $\widehat{\mathbf{X}} = \mathbf{x}/\lambda_{\text{max}}$ ,  $\widehat{H} = h(\mathbf{x}, t)/h_o$ ,  $\widehat{D} = d_o/h_o$  and  $\widehat{\tau} = u_c t/\lambda_{\text{max}}$  where  $u_c$  is the characteristic fluid speed based on in-plane thermocapillary flow [32]. The evolution of the liquid nanofilm is therefore controlled by two dimensionless numbers, namely a modified Capillary number  $\widehat{C}\widehat{a} = \mu u_c / \epsilon^3 \gamma_o$  and a modified Marangoni number  $\widehat{M}\widehat{a} = \epsilon \gamma_T \Delta T / \mu u_c$ . These numbers differ from their usual definitions by factors of the small parameter  $\epsilon = h_o/\lambda_{\text{max}}$  intrinsic to the long wavelength approximation. (This parameter should not be confused with the small parameter  $\epsilon$  pertaining to temporal behavior introduced in section 5.)

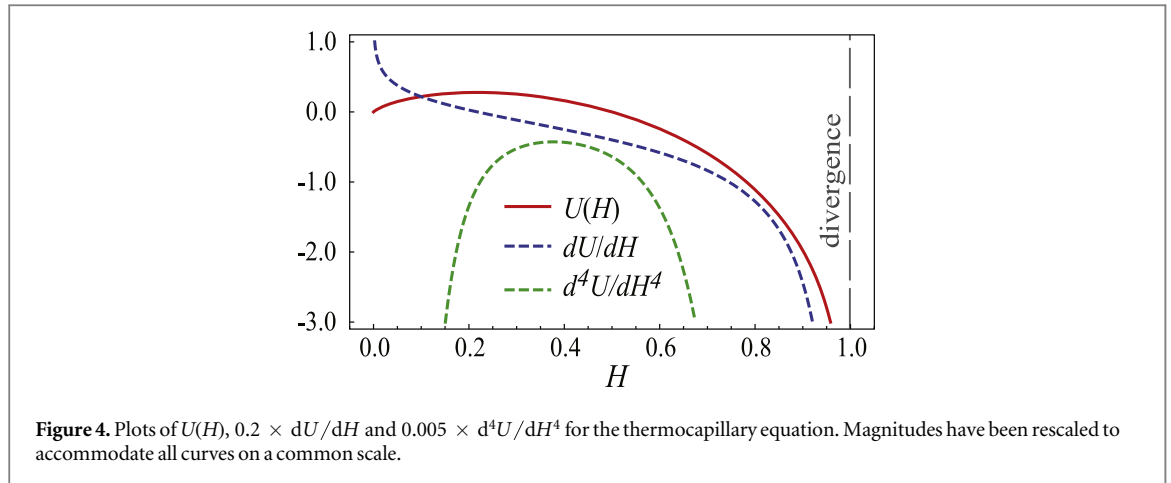
As evident, equation (3) exhibits a virtual singularity at  $H_s = \widehat{D}/(1 - \kappa)$  (or  $h = d_o/(1 - \kappa)$  in dimensional variables). This singularity lies outside the physical domain beyond the top cold substrate since  $\kappa < 1$ . For purposes of this current study, it proves convenient to recast equation (3) into parameter-free form such that

$$\frac{\partial H}{\partial \tau} + \nabla_{\parallel} \cdot \left[ H^3 \nabla_{\parallel} \nabla_{\parallel}^2 H + \frac{H^2}{(1 - H)^2} \nabla_{\parallel} H \right] = 0 \quad (4)$$

where  $H = \widehat{H}/H_s$ ,  $\mathbf{X} = \widehat{\mathbf{X}}/X_c$ ,  $\nabla_{\parallel} = X_c \widehat{\nabla}_{\parallel}$  and  $\tau = \widehat{\tau}/\tau_c$ . The reduced scalings are given by  $X_c = (2\widehat{D}H_s/3\kappa\widehat{M}\widehat{a}\widehat{C}\widehat{a})^{1/2}$  and  $\tau_c = 4\widehat{D}^2/(3\kappa^2H_s\widehat{M}\widehat{a}^2\widehat{C}\widehat{a})$ . In this final form, the top cold substrate is located at  $H = 1 - \kappa$  while the virtual singularity occurs at  $H = 1$ . In this work, we establish that the conical tip at the apex of the evolving cuspidal shape undergoes self-similar sharpening characterized by distinct power law exponents. Extraction of robust exponents, however, requires growth over several decades in time. We therefore focus on systems parametrized by  $\kappa \simeq 2 \times 10^{-4}$  in order to allow longer evolution times.

### 3. Stability considerations by analogy to gradient flows

In previous work [31, 32], we presented the linear stability analysis of equation (3) which exclusively focused on early time behavior of infinitesimal fluctuations in interfacial temperature or film thickness. That analysis



showed that the instability is of Type II [39] where all modal fluctuations of wavelength  $\lambda > \lambda_{\max}/\sqrt{2}$  are linearly unstable irrespective of the magnitude  $\Delta T$ . Eliciting the stability characteristics of stationary states of the full nonlinear equation given by equation (4) requires a different approach based on the system free energy  $\mathfrak{F}[H]$ . By exploiting an analogy to general gradient flows, we show next that equation (4) does not admit any stable stationary states on periodic or infinite (lateral) domains so long as  $H > 0$ .

Mitlin [40] has previously shown that the interface equation describing thin film dewetting by van der Waals forces, the process depicted in figures 1(a) and (b), can be rewritten in Cahn–Hilliard form described by

$$\partial H/\partial \tau = \nabla_{\parallel} \cdot [M(H)\nabla_{\parallel}(\delta\mathfrak{F}/\delta H)], \quad (5)$$

known more generally as gradient flow form [41]. The thermocapillary model described by equation (4) can also be written in this form where the free energy functional is given by

$$\mathfrak{F}[H, p] = \int_{\Omega} \left( \frac{1}{2} |\nabla_{\parallel} H|^2 + U(H) \right) d\Omega - p \left( \int_{\Omega} H d\Omega - V \right), \quad (6)$$

with mobility coefficient  $M(H) = H^3$ , potential function  $U(H) = H \ln[(1 - H)/H]$  and  $\delta\mathfrak{F}/\delta H = -\nabla_{\parallel}^2 H + dU/dH$ . The curves in figure 4 show that  $U(H)$  has no global minimum (and that  $U(H)$ ,  $dU/dH$  and  $d^4U/dH^4$  all diverge at the virtual singularity  $H = 1$ ). The energy of the thin film system depends, of course, on the total liquid volume  $V$  assumed here to be a conserved quantity. The constraint that the total volume  $V = \int_{\Omega} \bar{H} d\Omega$  remain constant is enforced through the Lagrange multiplier constant  $p$ . As shown in appendix A,  $d\mathfrak{F}/d\tau \leq 0$  for any lateral periodic domain  $\Omega$ . The proof for a lateral infinite domain simply requires that the integrand in equation (6) be augmented by the term  $U[H(X \rightarrow \infty, \tau)]$ , but otherwise proceeds similarly.

We consider stationary solutions  $\bar{H}$  represented by the extrema of equation (6) which satisfy  $\delta\mathfrak{F}[\delta H, \delta p; \bar{H}, p] = 0$  for infinitesimal variations  $\delta H$  and  $\delta p$ . This yields the value of the Lagrange multiplier

$$p = \left( -\nabla_{\parallel}^2 H + \frac{dU}{dH} \right)_{H=\bar{H}}, \quad (7)$$

which defines the surface pressure required for maintaining stationary states of constant volume  $V$ . It has previously been shown that for a general class of thin film equations [42] which include the form of equation (4), small perturbations to periodic stationary states (i.e.  $\delta H \propto \partial^2 \bar{H}/\partial X^2$ ) lead to negative values of the second variation

$$\delta^2 \mathfrak{F}[\delta H, \delta p; \bar{H}, p] = \int_{\Omega} |\nabla_{\parallel} \delta H|^2 + \frac{d^2 U}{dH^2} \Big|_{\bar{H}} \delta H^2 d\Omega < 0 \quad (8)$$

whenever the potential function satisfies the relation  $d^4U/dH^4|_{H=\bar{H}} < 0$ . This negative value indicates that there are always nearby states with same periodicity as  $\bar{H}$  but of lower free energy. The proof of this is outlined in appendix B. Since for the thermocapillary model the curve  $d^4U/dH^4$  in figure 4 is always negative, equation (4) cannot therefore support any stable stationary periodic states. This analysis is quite general and can be applied to many other thin film systems (even volume non-conserving systems) so long as the governing interface equation can be cast into the form of equation (5).

## 4. Numerical solution of nonlinear thermocapillary equation

To gain further insight into the behavior of equation (4) for growth in the nonlinear regime, we examine details of the dynamical shapes obtained from numerical solutions for rectilinear  $[H(X, \tau)]$  and cylindrical  $[H(R, \tau)]$  geometry. By virtue of the fact that vertical dimensions cannot exceed the substrate separation distance and that lateral dimensions continue to scale with the dominant wavelength of the initial instability, the results below rigorously satisfy the lubrication approximation throughout the cuspidal formation process. (This is in contrast with other thin film problems which involve asymptotic matching to regions described by a Stokes flow [43].) A mixed Lagrange finite element method [44] was used to evolve the solutions, subject to no-flux conditions at the boundaries of the lateral domain  $[0, \lambda_{\max}/2]$  and initial condition  $H(X, \tau = 0) = 1/3 \times [1 + 0.1 \cos(2\pi X/\lambda_{\max})]$  (with  $X$  replaced by  $R$  for cylindrical geometry). The restriction to a domain size  $\lambda_{\max}/2$  ensured that the dynamics of an individual cuspidal shape could be examined with high resolution without interference from similar adjacent shapes arising from the native linear instability discussed in section 2. Quadratic elements numbering about 20,000 and of minimum size  $4 \times 10^{-8}$  ensured sufficient spatial resolution of the emerging cuspidal region. The mesh sizes were everywhere much smaller than  $|\nabla_{\parallel}^2 H|^{-1}$  at all times. Integration in time relied on a second order backward difference scheme with small adaptive time stepping. Typically, full evolution toward the asymptotic shapes required about 11 000 integration steps. Simulations were terminated when the (dimensionless) distance between the virtual singularity at  $H = 1$  and the liquid cusp apex  $H_{\text{apex}}(\tau) = H(0, \tau)$  reached a value of about  $10^{-4}$ .

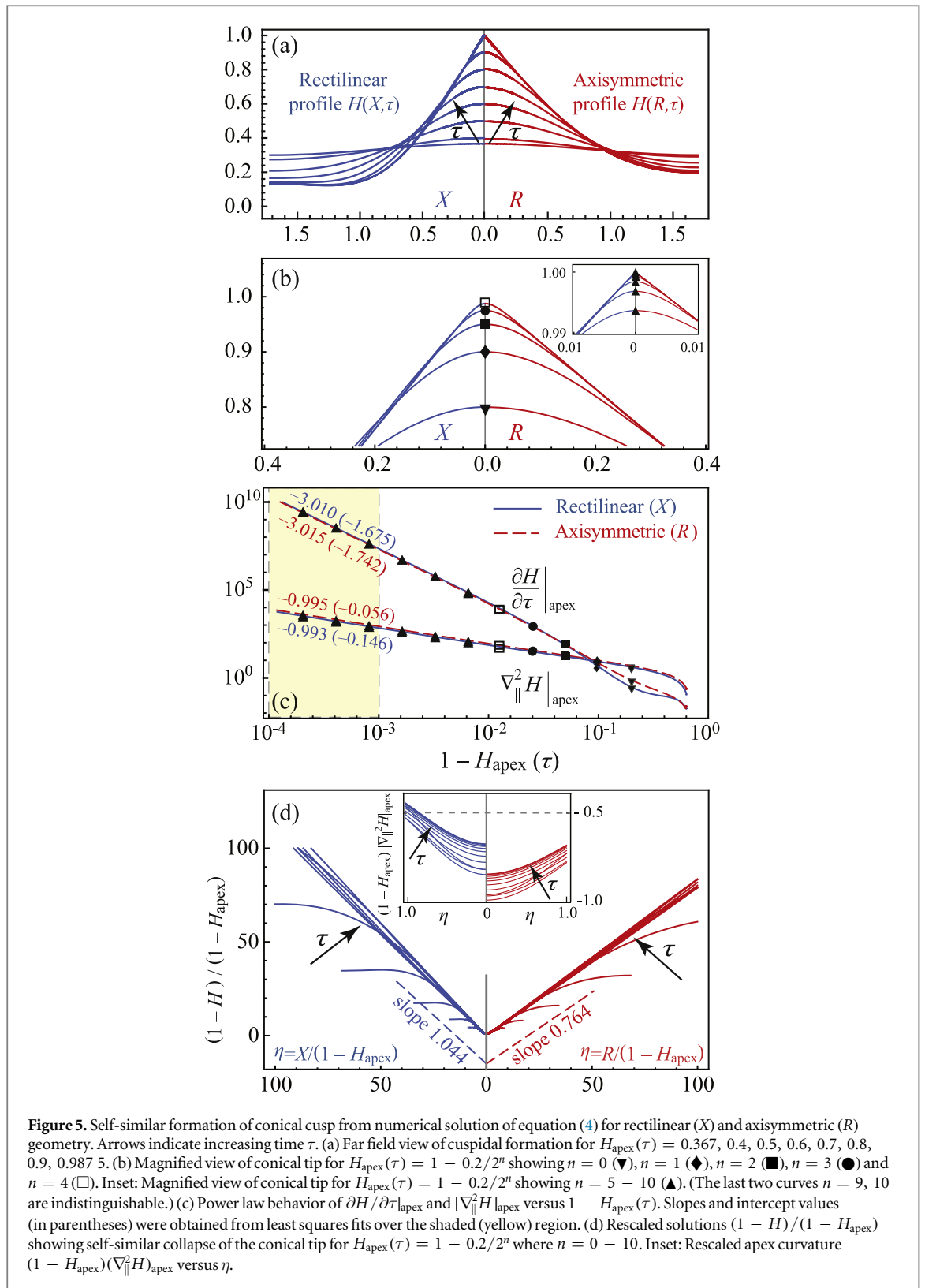
Shown in figure 5 are far field (a) and magnified views (b) of an evolving cusp capped by a conical tip. As expected from consideration of volume accumulation, the rectilinear geometry leads to a slightly thinner cusp for the same time interval. Inspection of the shape of the fluid tip reveals a conical protrusion with constant slope whose tip radius decreases rapidly in time. Plotted in figure 5(c) are the tip speed  $\partial H/\partial \tau|_{\text{apex}}$  and magnitude of the tip curvature  $|\nabla_{\parallel}^2 H|_{\text{apex}}$  as a function of the decreasing distance  $1 - H_{\text{apex}}(\tau)$ . The power law behavior observed persists for almost four decades in time indicating robust self-similar growth. The indicated asymptotic values for the slope and intercept values (in parentheses) of the lines shown were obtained from least squares fits over the shaded (yellow) portion shown. This self-similar behavior confirms the relations  $\partial H_{\text{apex}}/\partial \tau \sim (1 - H_{\text{apex}})^{-3}$  and  $(\nabla_{\parallel}^2 H)_{\text{apex}} \sim (1 - H_{\text{apex}})^{-1}$ . Introducing the singular time  $\tau_s$  where  $H_{\text{apex}} = 1$ —the singular point of equation (4)—yields the scaling relations governing the conical tip region, namely  $(1 - H_{\text{apex}})/(\tau_s - \tau) \sim (1 - H_{\text{apex}})^{-3}$  and  $(1 - H_{\text{apex}})/X^2 \sim (1 - H_{\text{apex}})^{-1}$ . These reveal the self-similar variables characterizing this asymptotic regime, namely  $X \sim 1 - H_{\text{apex}} \sim (\tau_s - \tau)^{1/4}$ , which reflect the lack of an intrinsic spatial or temporal scale in the conical region. As evident in figure 5(d), the shape of the conical tip undergoes collapse onto a common curve when both the vertical and lateral dimensions are normalized by the factor  $(1 - H_{\text{apex}})$ . The extent of the collapsed region is observed to increase in time. Shown in the inset of figure 5(d) is the rescaled apical curvature  $(1 - H_{\text{apex}})(\nabla_{\parallel}^2 H)_{\text{apex}}$  versus  $\eta = (X, R)/(1 - H_{\text{apex}})$ , which also exhibits self-similar collapse. The virtual singularity  $H_{\text{apex}} = 1$  appears therefore to act as an attractor state for formation of the conical tip.

The top panel shown in figure 6 represents 3D views of an evolving cusp with a conical tip at for the four times designated, as obtained from finite element simulation of the full nonlinear equation (4). The accompanying supplementary material available online at [stacks.iop.org/NJP/21/013018/mmedia](https://stacks.iop.org/NJP/21/013018/mmedia) contains additional information about the simulation including a video clip of the process. The bottom panel displays the value of the curvature of the gas/liquid interface at every point within the computational domain. The orange curves delineate concave from convex regions. The last image in the bottom panel clearly reveals that the interface evolves into a cuspidal shape capped by a conical tip with shrinking radius flanked by a broader convex surface.

We verified that these results converged upon mesh refinement and that the minimum mesh size chosen was sufficient to capture the dynamics of the evolving tip with high resolution. In particular, the scaling relations noted above establish constraints on the minimum mesh size  $\delta X \sim 1 - H_{\text{apex}} \sim 1/(\nabla_{\parallel}^2 H)_{\text{apex}}$  required to resolve the curvature in the apical region. For the results shown in figure 5, the simulations were terminated when  $1 - H_{\text{apex}} \sim O(10^{-4})$ . The minimum element size used of  $4 \times 10^{-8}$  ensured that  $\delta X \sim O(10^{-8}) \ll 1 - H_{\text{apex}}$ . We also estimated the error in the curvature term  $(\nabla_{\parallel}^2 H)_{\text{apex}}$  as follows. For rectilinear geometry for example, the finite element discretization of the Laplacian is analogous to the expression for the central finite difference technique. Letting  $D_{\parallel}^2$  denote the finite difference approximation to the Laplacian, the local truncation error is therefore given by

$$D_{\parallel}^2 H = \nabla_{\parallel}^2 H + O(\delta X^2, \nabla_{\parallel}^2 \nabla_{\parallel}^2 H). \quad (9)$$

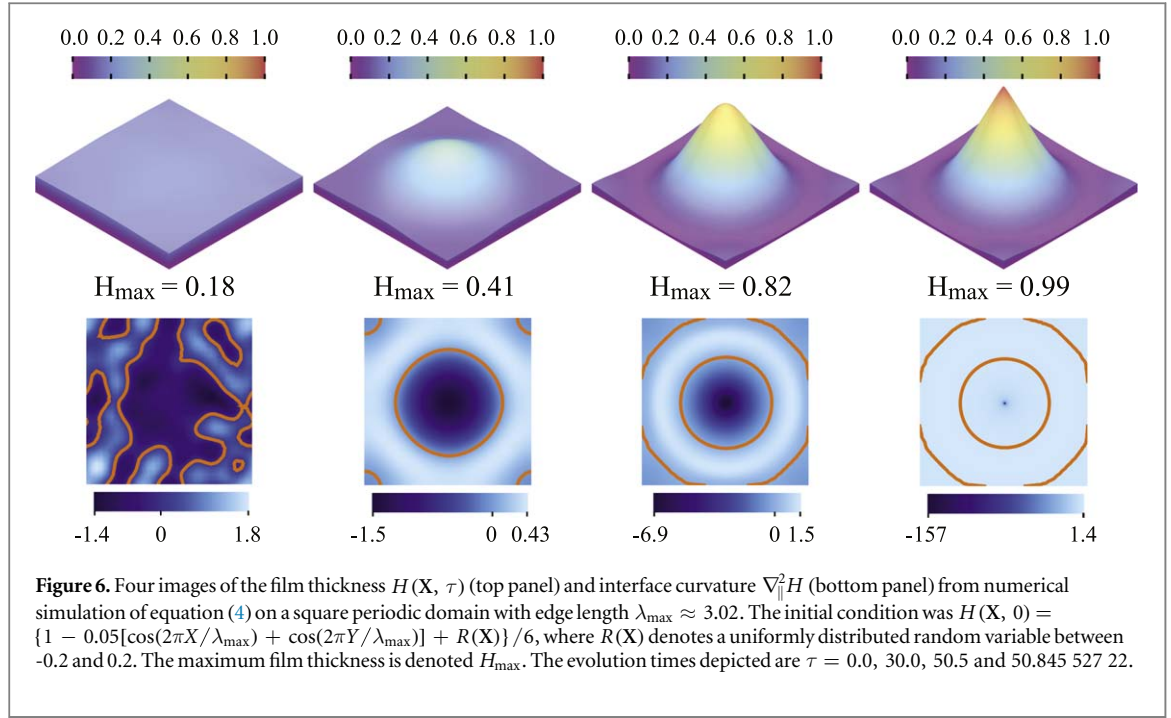
From the scaling relation above, the error  $(\nabla_{\parallel}^2 \nabla_{\parallel}^2 H)_{\text{apex}}$  is expected to be  $O((1 - H_{\text{apex}})^{-3}) \sim O(10^{12})$  and since  $\delta X \sim O(10^{-8})$ , the error  $O(\delta X^2) \sim O(10^{-16})$ . Therefore, the overall local error in  $(\nabla_{\parallel}^2 H)_{\text{apex}} \sim O(10^{-4})$  was sufficiently small in our simulations to capture with high resolution the self-similar dynamics in the apical region before the simulations were terminated to prevent contact with the top colder substrate.



### 5. Asymptotic analysis of self-similar cusp formation

The exponents obtained from these numerical simulations were also confirmed by analysis of equation (4) by considering a Taylor expansion about the virtual singular point  $H = 1$ , which yields the asymptotic evolution equation





$$\frac{\partial H}{\partial \tau} + \nabla_{\parallel} \cdot \left[ \nabla_{\parallel} \nabla_{\parallel}^2 H + \frac{1}{(1-H)^2} \nabla_{\parallel} H \right] + O(1-H)^{-1} = 0. \quad (10)$$

Balancing the first and second term with the second and third term yields the same asymptotic relation obtained previously, namely  $X \sim 1 - H_{\text{apex}} \sim (\tau_s - \tau)^{1/4}$ . These scalings suggest introduction of the stretched variables

$$\eta = \frac{X}{\varepsilon} \quad \text{or} \quad \frac{R}{\varepsilon} \quad \text{and} \quad 1 - H = \sum_{n=1}^{\infty} \varepsilon^n w_n(\eta) \quad \text{where} \quad \varepsilon = (\tau_s - \tau)^{1/4}. \quad (11)$$

We note here that if equation (4) were truly scale invariant, and not just asymptotically so as  $H_{\text{apex}} \rightarrow 1$ , the expansion in equation (11) would terminate at  $n = 1$ . The appearance of the  $1 - H$  term in the denominator of equation (4), however, precludes such global scaling and instead leads to multiscale expansions of the form:

$$\frac{\partial H}{\partial \tau} = \frac{1}{\varepsilon^4} \sum_{n=1}^{\infty} \varepsilon^n \mathcal{T}_n(w_1, \dots, w_n), \quad (12)$$

$$\nabla_{\parallel} \cdot (H^3 \nabla_{\parallel} \nabla_{\parallel}^2 H) = \frac{1}{\varepsilon^4} \sum_{n=1}^{\infty} \varepsilon^n \mathcal{S}_n(w_1, \dots, w_n), \quad (13)$$

$$\nabla_{\parallel} \cdot \left[ \frac{H^2}{(1-H)^2} \nabla_{\parallel} H \right] = \frac{1}{\varepsilon^4} \sum_{n=1}^{\infty} \varepsilon^n \mathcal{M}_n(w_1, \dots, w_n), \quad (14)$$

where the symbols  $\nabla_{\parallel}$ ,  $\nabla_{\perp}$  and  $\nabla_{\parallel}^2$  represent the appropriate forms of the gradient, divergence and Laplacian operators for rectilinear ( $X$ ) or cylindrical ( $R$ ) geometry. To leading order  $n = 1$ , equation (10) then reduces to the nonlinear, fourth order equation given by

$$\mathcal{T}_1(w_1) + \mathcal{S}_1(w_1) + \mathcal{M}_1(w_1) = 0, \quad (15)$$

where the operators  $\mathcal{T}_1$ ,  $\mathcal{S}_1$  and  $\mathcal{M}_1$  are defined as

$$\mathcal{T}_1(w_1) = \frac{1}{4} \left( w_1 - \eta \frac{dw_1}{d\eta} \right), \quad (16)$$

$$\mathcal{S}_1(w_1) = -\nabla_{\eta}^2 \nabla_{\eta}^2 w_1, \quad (17)$$

$$\mathcal{M}_1(w_1) = \nabla_{\eta}^2 \left( \frac{1}{w_1} \right). \quad (18)$$

Here and in what follows, operator subscripts denote differentiation with respect to the self similar variable  $\eta$  for rectilinear or cylindrical form. Required symmetry about the axis of origin yields two boundary conditions, namely  $(dw_1/d\eta)_{\eta=0} = 0$  and  $(d^3 w_1/d\eta^3)_{\eta=0} = 0$ . An additional boundary condition is obtained from the requirement that equation (12) remain bounded as  $\varepsilon \rightarrow 0$ , or equivalently as  $\eta \rightarrow \infty$ , which requires that the leading term  $\mathcal{T}_1$  vanish. This then leads to the Robin condition  $\mathcal{T}_1(w_1)|_{\eta \rightarrow \infty} = 0$ . To leading order then, the asymptotic solution to equation (15) is satisfied by the Laurent series

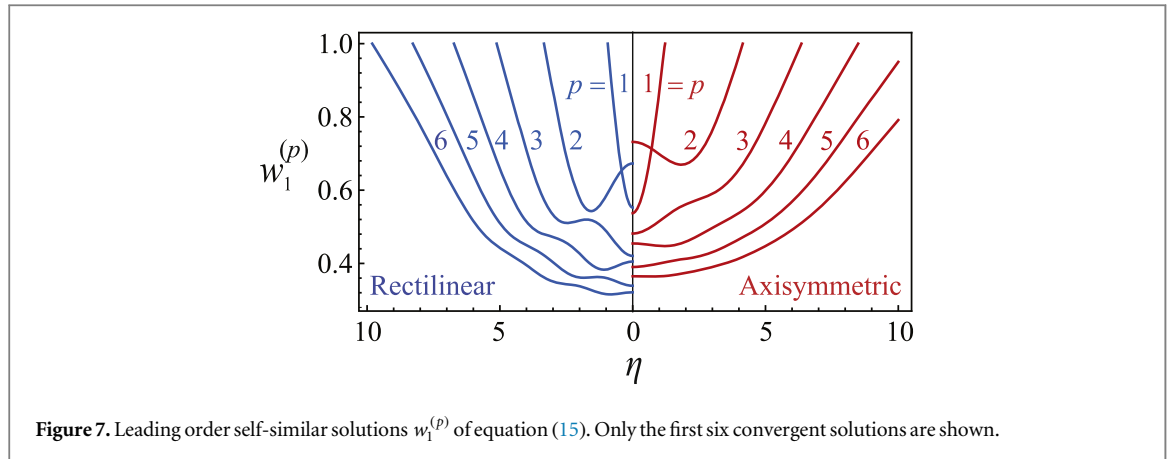


Figure 7. Leading order self-similar solutions  $w_1^{(p)}$  of equation (15). Only the first six convergent solutions are shown.

Table 1. Asymptotic values of the interface slope, apex height and apex curvature for the leading order solution  $w_1$  to equation (15). Numbers in blue and red denote values for rectilinear and axisymmetric geometry, respectively.

$p$	$\lim_{\eta \rightarrow \infty} dw_1^{(p)}/d\eta$	$w_1^{(p)}(0)$	$\nabla_\eta^2 w_1^{(p)}(0)$
1	1.0437 0.7639	0.5526 0.5372	1.2082 1.5563
2	0.3430 0.2474	0.6728 0.7317	-0.2316 -0.1624
3	0.2145 0.1610	0.4204 0.4816	0.2021 -0.1669
4	0.1580 0.1196	0.4052 0.4544	-0.0884 -0.0438
5	0.1257 0.0962	0.3390 0.3902	0.0792 0.0526
6	0.1046 0.0806	0.3211 0.3649	-0.0364 -0.0087

$$w_1^\infty = \sum_{n=1}^{\infty} a_n \eta^{5-4n} = a_1 \eta + O(\eta^{-3}) \quad \text{as } |\eta| \rightarrow \infty. \tag{19}$$

Convergence to  $w_1^\infty$  can be obtained by linearizing equation (15) about the solution  $w_1(\eta \rightarrow \infty) = w_1^\infty(\eta) + f(\eta)$  which yields the non-homogeneous linear equation

$$\mathcal{T}_1(f) + \mathcal{S}_1(f) - \nabla_\eta^2 (f/(w_1^\infty)^2) = 0. \tag{20}$$

In the limit  $|a_1| \ll 1$ , this equation leads to a singular perturbation problem whose inner region is influenced by the fourth order capillary term (not shown). Here we only focus on the global outer region solutions of the linearized equation obtained by WKBJ analysis where  $f(\sigma\eta) = \exp[\sigma^{-4/3} \sum_{n=0}^{\infty} \sigma^{4n/3} S_n(\sigma\eta)]$  for  $\sigma \ll 1$ . Matching terms of order  $\sigma^{-4/3}$  and  $\sigma^0$  and solving for the resulting two ordinary equations yields the form of the general solution

$$f \sim \beta_0 \eta + \sum_{n=1}^3 \frac{\beta_n}{\eta^\alpha} \exp\left[-\frac{3}{4^{4/3}} e^{2n\pi i/3} \eta^{4/3}\right] + \dots, \tag{21}$$

where  $\alpha = 1$  for rectilinear and  $\alpha = 5/3$  for axisymmetric geometry. To preclude the first two terms in the summation from undergoing divergent oscillatory behavior, it is required that  $\beta_1 = \beta_2 = 0$ . The two remaining non-vanishing terms proportional to  $\beta_0$  and  $\beta_3$  simply reflect an infinitesimal shift in the far field slope and a rapidly decaying function, respectively. Were the analytic solution to equation (15) known within the apical region, then the coefficients  $\beta_0$  and  $\beta_3$  could be obtained by asymptotic matching. Absent that information, the solutions to equation (15) are still constrained by the symmetry requirement about at the origin. This imposes the restriction that solutions can only be found for special values of the far field slope, as discussed next.

The numerical solutions to equation (15) were computed on a finite domain sufficiently long to preclude finite size effects; the results shown also converged upon mesh refinement. Shown in figure 7 are the first six similarity solutions with corresponding numerical values listed in table 1. The asymptotic interface slopes of the conical tip for axisymmetric geometry are always smaller than the slopes for rectilinear geometry, as expected. The axisymmetric solutions also display weaker oscillatory behavior, likely due to suppression by the capillary pressure associated with the additional term in the interface curvature. The fundamental mode  $p = 1$  exhibits no oscillatory behavior unlike the higher order solutions  $p \geq 2$ .

Next we compare the fitting coefficients from the asymptotic self-similar analysis of equation (15) with those obtained from direct numerical simulations of equation (4), which are plotted in figure 5. To leading order

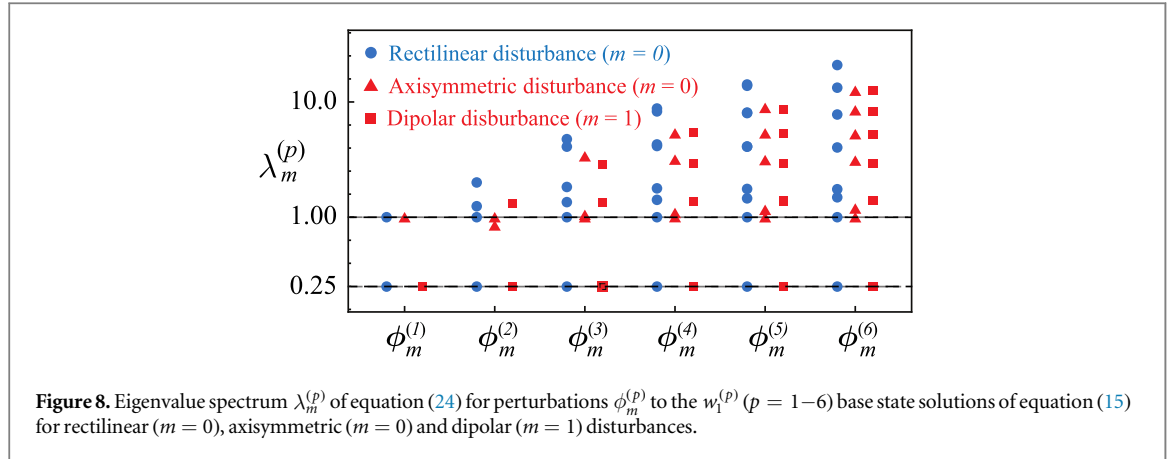


**Figure 8.** Eigenvalue spectrum  $\lambda_m^{(p)}$  of equation (24) for perturbations  $\phi_m^{(p)}$  to the  $w_1^{(p)}$  ( $p = 1-6$ ) base state solutions of equation (15) for rectilinear ( $m = 0$ ), axisymmetric ( $m = 0$ ) and dipolar ( $m = 1$ ) disturbances.

$1 - H_{\text{apex}} \approx \varepsilon w_1^{(p)}(0)$ , it can be shown that the intercept value for  $(\partial H / \partial \tau)_{\text{apex}}$  is approximately  $4 \log_{10}[w_1^{(p)}(0)] - \log_{10} 4$  and for  $(\nabla_{\parallel}^2 H)_{\text{apex}}$  approximately  $\log_{10}[w_1^{(p)}(0) \nabla_{\parallel}^2 w_1^{(p)}(0)]$ . Substitution of the values for  $p = 1$  from table 1 into these expressions yields intercept values for  $(\partial H / \partial \tau)_{\text{apex}}$  equal to  $-1.632$  (rectilinear) and  $-1.681$  (axisymmetric). Likewise, the intercept values for  $(\nabla_{\parallel}^2 H)_{\text{apex}}$  equal  $-0.175$  (rectilinear) and  $-0.078$  (axisymmetric). These predicted values are in excellent agreement with the numerical intercept values (shown in parentheses) in figure 5(c). Additionally, the asymptotic values of the interface slope  $\lim_{\eta \rightarrow \infty} dw_1^{(1)} / d\eta$  given in table 1 show excellent agreement when superposed on the profiles in figure 5(d). The asymptotic values are predicted to be 1.043 7 (rectilinear) and 0.763 9 (axisymmetric), while the numerical results yielded 1.044 and 0.764. Converting back to dimensional form, the value of conical tip slope is given by the relation

$$\text{Conical tip slope} = (\gamma_T \Delta T / \gamma_0)^{1/2} [3\kappa / 2(1 - \kappa)]^{1/2} \times \lim_{\eta \rightarrow \infty} dw_1^{(1)} / d\eta. \quad (22)$$

In section 4, it was shown that the numerical solution to the full nonlinear equation given by equation (4) asymptotes to a fluid elongation resembling a cuspidal shape capped by a conical tip. The asymptotic analysis in this section reveals that the numerical solution for this shape corresponds identically to the fundamental solution  $w_1^{(1)}$ . A general proof of why the numerical solution always converges to this fundamental solution and not other solutions  $w_1^{(p \geq 2)}$  is beyond the scope of this work. Further examination of this finding by implementing a conventional linear stability analysis of equation (10) is a non-trivial exercise because of the multiscale nature of the self-similar base state solutions, which evolve on multiple time scales  $\{\varepsilon^n\}_{n=1}^{\infty}$ . However, since both the numerical and analytic solutions suggest that the late stage dynamics of equation (11) is dominated by the term  $w_1^{(p)}$ , it suffices then to consider infinitesimal perturbations described by

$$1 - H = \varepsilon w_1^{(p)}(\eta) + \varepsilon^{1-4\lambda} \sum_{m=0}^{\infty} e^{im\theta} \phi_m^{(p)}(\eta), \quad (23)$$

where  $|\phi_m^{(p)}(\eta)| \ll 1$  denotes an infinitesimal modal perturbation to  $w_1^{(p)}(\eta)$ ,  $\theta$  is the polar angle in cylindrical coordinates, and  $\varepsilon$  is defined in equation (11). The resulting eigenvalue problem is given by

$$\mathcal{T}_1[\phi_m^{(p)}] + \mathcal{S}_1[\phi_m^{(p)}] + \delta \mathcal{M}_1[\phi_m^{(p)}] = \lambda_m^{(p)} \phi_m^{(p)}, \quad (24)$$

where  $\delta \mathcal{M}_1[\phi_m^{(p)}] = -\nabla_{(\eta, \theta)}^2 [\phi_m^{(p)} / (w_1^{(p)})^2]$  and where  $\nabla_{(\eta, \theta)}^2$  denotes the Laplacian with regard to  $\eta$  and the angular coordinate  $\theta$ . (The differential operators in equation (15) must also be expanded to include the the angular dependence on  $\theta$ .) In order for localized perturbations in the far field to preserve constant slope, it is required that  $\mathcal{T}_1[\phi_m^{(p)}] - \lambda_m^{(p)} \phi_m^{(p)} \rightarrow 0$  as  $\eta \rightarrow \infty$ . Here, positive eigenvalues  $\lambda_m^{(p)}$  reflect perturbations  $\phi_m^{(p)}$  with algebraic growth  $(\tau_s - \tau)^{1-4\lambda}$ , which is faster than the growth  $(\tau_s - \tau)^{1/4}$  of the corresponding base state solutions  $w_1^{(p)}$ . We also note that since equation (10) is both space and time translationally invariant, then for each value of  $p$  there must exist two eigenvalues reflecting these symmetries, namely the eigenfunction  $\cos \theta \times dw_1^{(p)} / d\eta$  with eigenvalue  $1/4$  and the eigenfunction  $(w_1^{(p)} - \eta dw_1^{(p)} / d\eta) / 4$  with eigenvalue 1, respectively.

Plotted in figure 8 is the eigenvalue spectrum  $\lambda_m^{(p)}$  for infinitesimal modal perturbations  $\phi_m^{(p)}$  for the first six self-similar base state solutions  $w_1^{(p)}$  where  $p = 1-6$ . Each solution contains  $2p$  eigenvalues. Irrespective of the geometry, the fundamental solution  $w_1^{(1)}$  is the only solution with no positive eigenvalues aside from  $1/4$  and 1. The solution  $w_1^{(1)}$  is therefore the only solution that is linearly stable to perturbations. The remaining positive eigenvalues increase in magnitude with increasing  $p$ , indicating more rapid growth and instability associated with the coefficient  $\varepsilon^{1-4\lambda}$  multiplying the last term in equation (23). The numerical simulations described in section 4 and plotted in figures 5 and 6 were always found to asymptote to the bounded fundamental solution

$w_1^{(1)}$ . Similar strong convergence to the stable fundamental solution has previously been reported for the thin film equation describing van der Waals rupture [45] (shown in figure 1). In that example, initialization of the thin film equation by the corresponding solution  $w_1^{(p \geq 2)}$  for that problem leads to a different global liquid film configuration—however, the local behavior in the vicinity of the line or point rupture converges to the fundamental mode  $w_1^{(1)}$ . A full investigation of the local scaling behavior leading to self-similar cuspidal formation in the thermocapillary system for initial conditions resembling higher order eigenmodes is left for further study. It is anticipated that irrespective of the initial condition, simulation of the full nonlinear evolution equation given by equation (4) will still yield film shapes dominated by  $w_1^{(1)}$  in the region of the conical tip since  $w_1^{(1)}$  is found to be linearly stable.

## 6. Conclusion

The analysis and simulations presented in this work reveal how surface shear forces due to runaway thermocapillary stresses generate fluid protrusions resembling cuspidal shapes capped by a conical tip. This finding expands the category of hydrodynamic flows known to form stable cuspidal shapes to include thin film systems subject to interfacial shear, where the driving force is oriented parallel to the moving interface. The asymptotic analysis reveals how the conical tip undergoes self-focusing toward a virtual attractor state characterized by a line (rectilinear case) or point (axisymmetric case) singularity via a robust self-similar process. The asymptotic derivation also yields an analytic relation for the slope of the conical tip which should prove useful to experimentalists who wish to design microarrays with specified tip slopes for beam shaping, antireflective coatings or other textured substrates.

The original system described, based on a thin uniform molten film confined by parallel solid boundaries maintained at different uniform temperature, is known to support a linear instability that forms arrays of rounded protrusions resembling microlenses. These protrusions are expected to evolve into arrays of cuspidal shapes with conical tips by the nonlinear dynamical process described since the thermal gradient across the gas layer just above the fluid tip progressively increases in time, leading to a runaway process. We anticipate that any initial film configuration that contains local maxima in film thickness, whether or not periodically arranged and however initially seeded, will also trigger cusp formation at such locations given the local, self-similar nature of the underlying growth process. We also anticipate that evaporative effects [46] in nanofilms containing volatile components which require that the temperature of the warmer substrate exceed the vapor saturation temperature, an effect not considered in this work, may preclude self-similarity in the apical region.

We have previously shown [30, 36–38] that the evolution process leading to rounded lenslet microarrays can be terminated on demand and the liquid shapes affixed in place by dropping the temperature of both substrates below the solidification point. Rapid solidification of these liquid structures is made possible by two advantageous features: the large surface to volume ratios intrinsic to microscale or nanoscale films which facilitates rapid cooling, and digital control over the temperature of the confining substrates. We fully expect that similar rapid solidification can be achieved once the desired conical protrusions have formed in order to solidify and affix their shape on demand. Perhaps alternative methods of flow control by laser manipulation, previously applied to thin film thermocapillary spreading along a solid substrate, can also be used [47]. In summary, we hope the theoretical analysis provided here helps guide development of a novel lithographic method for direct, non-contact fabrication of cuspidal microarrays, whose shapes would be more difficult, costly or even impossible to fabricate by other means.

## Appendix A. Proof of relation $d\mathfrak{F}[H]/d\tau \leq 0$

We evaluate the quantity  $d\mathfrak{F}[H]/d\tau$  for the free energy  $\mathfrak{F}[H]$  defined in equation (6) by applying Leibnitz's rule for differentiation over a fixed periodic domain  $\Omega$ :

$$\frac{d\mathfrak{F}[H]}{d\tau} = \frac{d}{d\tau} \int_{\Omega} \left( \frac{1}{2} |\nabla_{\parallel} H|^2 + U(H) \right) d\Omega \quad (\text{A.1})$$

$$= \int_{\Omega} \left( \nabla_{\parallel} H \cdot \frac{\partial}{\partial \tau} (\nabla_{\parallel} H) + \frac{dU}{dH} \frac{\partial H}{\partial \tau} \right) d\Omega. \quad (\text{A.2})$$

Interchanging the order of operators  $\nabla_{\parallel}$  and  $\partial/\partial\tau$  and applying Green's first identity to the first integral in equation (A.2) gives

$$\frac{d\mathfrak{F}[H]}{d\tau} = \int_{\Omega} \left( -\nabla_{\parallel}^2 H + \frac{dU}{dH} \right) \frac{\partial H}{\partial \tau} d\Omega, \quad (\text{A.3})$$

where continuity of  $H$  and higher order derivatives ensures that the boundary term proportional to  $\nabla_{\parallel} H$  vanishes identically. Substitution of the term  $\partial H / \partial \tau$  in equation (A.3) by the relations given in equation (5) and equation (6) yields

$$\frac{d\mathfrak{F}[H]}{d\tau} = \int_{\Omega} \left( -\nabla_{\parallel}^2 H + \frac{dU}{dH} \right) \nabla_{\parallel} \cdot \left\{ M(H) \nabla_{\parallel} \left( -\nabla_{\parallel}^2 H + \frac{dU}{dH} \right) \right\} d\Omega, \quad (\text{A.4})$$

where  $M(H) = H^3$ . Application of Green's first identity subject to the vanishing boundary term yields the desired inequality

$$\frac{d\mathfrak{F}[H]}{d\tau} = - \int_{\Omega} \left\{ M(H) \left| \nabla_{\parallel} \left( -\nabla_{\parallel}^2 H + \frac{dU}{dH} \right) \right|^2 \right\} d\Omega \leq 0. \quad (\text{A.5})$$

## Appendix B. Proof of relation $\delta^2 \mathfrak{F}[\delta H, \delta p; \bar{H}, p] < 0$

We consider the free energy associated with a small deviation about a stationary solution  $\bar{H}$  of equation (6) for arbitrary perturbation  $\delta H$ :

$$\mathfrak{F}[\bar{H} + \delta H] = \mathfrak{F}[\bar{H}] + \delta \mathfrak{F}[\delta H, \delta p; \bar{H}, p] + \frac{1}{2} \delta^2 \mathfrak{F}[\delta H, \delta p; \bar{H}, p] + O(\delta H)^3. \quad (\text{B.1})$$

By definition, the first variation of the energy  $\delta \mathfrak{F}[\delta H, \delta p; \bar{H}, p]$  must vanish identically for any such stationary solution  $\bar{H}$ . Here, the second variation is given by the integral quantity

$$\delta^2 \mathfrak{F}[\delta H, \delta p; \bar{H}, p] = \int_{\Omega} |\nabla_{\parallel} \delta H|^2 + \frac{d^2 U}{dH^2} \Big|_{\bar{H}} \delta H^2 - 2 \delta p \delta H \, d\Omega \quad (\text{B.2})$$

subject to the constraint of constant volume  $V$  such that

$$\int_{\Omega} (\bar{H} + \delta H) \, d\Omega = V, \quad (\text{B.3})$$

which requires therefore that  $\int_{\Omega} \delta H \, d\Omega = 0$ . This in turn indicates that the integrated value of the last term in equation (B.2) reduces to zero. Application of Green's first identify reduced the second variation  $\delta^2 \mathfrak{F}$  to the form

$$\delta^2 \mathfrak{F}[\delta H, \delta p; \bar{H}, p] = \int_{\Omega} \delta H \times \left( -\nabla_{\parallel}^2 \delta H + \frac{d^2 U}{dH^2} \Big|_{\bar{H}} \delta H \right) d\Omega, \quad (\text{B.4})$$

where the additional boundary integral vanishes identically for any periodic perturbation  $\delta H$ .

It is now a straightforward exercise to show that there always exist admissible arbitrary perturbations  $\delta H$  such that  $\delta^2 \mathfrak{F}[\delta H, \delta p; \bar{H}, p]$  is always strictly negative. We recall from equation (7) that the interfacial pressure  $p$  (i.e. Lagrange multiplier) corresponding to a stationary state  $\bar{H}$  of volume  $V$  is given by

$$p = \left( -\nabla_{\parallel}^2 H + \frac{dU}{dH} \right)_{H=\bar{H}}. \quad (\text{B.5})$$

Differentiating equation (B.5) twice with respect to  $X$  yields the relation

$$-\nabla_{\parallel}^2 \frac{\partial^2 \bar{H}}{\partial X^2} + \frac{d^2 U}{dH^2} \Big|_{\bar{H}} \frac{\partial^2 \bar{H}}{\partial X^2} = - \frac{d^3 U}{dH^3} \Big|_{\bar{H}} \left( \frac{\partial \bar{H}}{\partial X} \right)^2. \quad (\text{B.6})$$

Substituting equations (B.6) into (B.4) for perturbations of the form  $\delta H = \partial^2 \bar{H} / \partial X^2$  with vanishing total volume yields

$$\delta^2 \mathfrak{F}[\delta H, \delta p; \bar{H}, p] = - \int_{\Omega} \left( \frac{\partial^2 \bar{H}}{\partial X^2} \right) \frac{d^3 U}{dH^3} \Big|_{\bar{H}} \left( \frac{\partial \bar{H}}{\partial X} \right)^2 d\Omega \quad (\text{B.7})$$

$$= - \int_{\Omega} \frac{d^3 U}{dH^3} \Big|_{\bar{H}} \frac{1}{3} \frac{\partial}{\partial X} \left( \frac{\partial \bar{H}}{\partial X} \right)^3 d\Omega \quad (\text{B.8})$$

$$= \frac{1}{3} \int_{\Omega} \left( \frac{d^4 U}{dH^4} \Big|_{\bar{H}} \frac{\partial \bar{H}}{\partial X} \right) \left( \frac{\partial \bar{H}}{\partial X} \right)^3 d\Omega \quad (\text{B.9})$$

$$= \frac{1}{3} \int_{\Omega} \left( \frac{\partial \bar{H}}{\partial X} \right)^4 \frac{d^4 U}{dH^4} \Big|_{\bar{H}} d\Omega. \quad (\text{B.10})$$

All boundary terms from integrations by parts vanish due to periodic boundary conditions. For the thermocapillary model described by equation (6), the potential function  $U(H) = H \ln[(1 - H)/H]$  for

$H \in (0, 1)$  and therefore

$$\frac{d^4U}{dH^4} = -\frac{2(1-2H)^2 + 4H^2}{H^3(1-H)^4} < 0. \quad (\text{B.11})$$

When substituted into equation (B.10), this yields the relation  $\delta^2\mathfrak{F}[\delta H, \delta p; \bar{H}, p] < 0$ . This inequality assures that for every nonuniform stationary state  $\bar{H}$  such that  $\partial H/\partial X$  is not everywhere zero, there always exists a neighboring state  $\bar{H} + \delta H$  of lower free energy.

## References

- [1] Mullins W W 1957 Theory of thermal grooving *J. Appl. Phys.* **28** 333–9
- [2] Bernoff A J, Bertozzi A L and Witelski T P 1998 Axisymmetric surface diffusion: dynamics and stability of self-similar pinchoff *J. Stat. Phys.* **93** 725–76
- [3] Schwabe M, Rubin-Zuzic M, Zhdanov S, Ivlev A, Thomas H M and Morfill G E 2009 Formation of bubbles, blobs, and surface cusps in complex plasmas *Phys. Rev. Lett.* **103** 114501
- [4] Yang Z H, Maitra N T and Burke K 2012 Effect of cusps in time-dependent quantum mechanics *Phys. Rev. Lett.* **108** 063003
- [5] Amiranashvili S, Bandelow U and Akhmediev N 2011 Dispersion of nonlinear group velocity determines shortest envelope solitons *Phys. Rev. A* **84** 043834
- [6] Burton J C and Taborek P 2011 Simulations of coulombic fission of charged inviscid drops *Phys. Rev. Lett.* **106** 144501
- [7] Kolvin I, Cohen G and Fineberg J 2015 Crack front dynamics: the interplay of singular geometry and crack instabilities *Phys. Rev. Lett.* **114** 175501
- [8] Xiao Z, Zhang J, Sornborger A T and Tao L 2017 Cusps enable line attractors for neural computation *Phys. Rev. E* **96** 052308
- [9] Burelbach J P, Bankoff S G and Davis S H 1988 Nonlinear stability of evaporating/condensing liquid films *J. Fluid Mech.* **195** 463–94
- [10] Eggers J and Fontelos M A 2015 *Singularities: Formation, Structure and Propagation* (Cambridge: Cambridge University Press)
- [11] Thete S S, Anthony C, Basaran O A and Doshi P 2015 Self-similar rupture of thin free films of power-law fluids *Phys. Rev. E* **92** 023014
- [12] Zhang W W and Lister J R 1999 Similarity solutions for van der waals rupture of a thin film on a solid substrate *Phys. Fluids* **11** 2454–62
- [13] Witelski T P and Bernoff A J 2000 Dynamics of three-dimensional thin film rupture *Physica D* **147** 155–76
- [14] Blanchette F and Zhang W W 2009 Force balance at the transition from selective withdrawal to viscous entrainment *Phys. Rev. Lett.* **102** 144501
- [15] Eggers J 1993 Universal pinching of 3d axisymmetric free-surface flow *Phys. Rev. Lett.* **71** 3458–60
- [16] Eggers J 2001 Air entrainment through free-surface cusps *Phys. Rev. Lett.* **86** 4290–3
- [17] Karpitschka S, Eggers J, Pandey A and Snoeijer J H 2017 Cusp-shaped elastic creases and furrows *Phys. Rev. Lett.* **119** 198001
- [18] Zhang W W 2004 Viscous entrainment from a nozzle: singular liquid spouts *Phys. Rev. Lett.* **93** 184502
- [19] Cohen I and Nagel S R 2002 Scaling at the selective withdrawal transition through a tube suspended above the fluid surface *Phys. Rev. Lett.* **88** 074501
- [20] Courrech du Pont S and Eggers J 2006 Sink flow deforms the interface between a viscous liquid and air into a tip singularity *Phys. Rev. Lett.* **96** 034501
- [21] Marin A G, Enriquez O R, Brunet P, Colinet P and Snoeijer J H 2014 Universality of tip singularity formation in freezing water drops *Phys. Rev. Lett.* **113** 054301
- [22] Peters I, Snoeijer J H, Daerr A and Limat L 2009 Coexistence of two singularities in dewetting flows: regularizing the corner tip *Phys. Rev. Lett.* **103** 114501
- [23] Villiermaux E and Almarcha C 2016 Node dynamics and cusps size distribution at the border of liquid sheets *Phys. Rev. Fluids* **1** 041902(R)
- [24] Krechetnikov R 2012 Structure of marangoni-driven singularities *Phys. Fluids* **24** 022111
- [25] Krechetnikov R 2015 Cusps and cuspidal edges at fluid interfaces: existence and application *Phys. Rev. E* **91** 043019
- [26] Nowlin K and LaJeunesse D R 2017 Fabrication of hierarchical biomimetic polymeric nanostructured surfaces *Mol. Syst. Des. Eng.* **2** 201–13
- [27] Southwell W H 1991 Pyramid-array surface-relief structures producing antireflection index matching on optical surfaces *J. Opt. Soc. Am. A* **8** 549–543
- [28] Weibler R J, Menyuk C R, Busse L E, Shaw L B, Sanghera J S and Aggarwal I D 2016 Optimized moth-eye anti-reflective structures for As<sub>2</sub>S<sub>3</sub> chalcogenide optical fibers *Opt. Exp.* **24** 258966
- [29] Wisdom K M, Watson J A, Qua X, Liua F, Watson G S and Chen C H 2013 Self-cleaning of superhydrophobic surfaces by self-propelled jumping condensate *Proc. Natl Acad. Sci.* **110** 7992–7
- [30] McLeod E and Troian S M 2011 One step non-contact fabrication of polymer microlens arrays by thermocapillary lithography *CLEO 2011—Laser Applications to Photonic Applications* (Washington, DC: Optical Society of America) p CML3
- [31] Dietzel M and Troian S M 2009 Formation of nanopillar arrays in ultrathin viscous films: the critical role of thermocapillary stresses *Phys. Rev. Lett.* **103** 074501
- [32] Dietzel M and Troian S M 2010 Mechanism for spontaneous growth of nanopillar arrays in ultrathin films subject to a thermal gradient *J. Appl. Phys.* **108** 074308
- [33] Dietzel M and Troian S M 2009 Thermocapillary patterning of nanoscale polymer films *Materials Systems and Processes for Three Dimensional Micro- and Nanoscale Fabrication and Lithography* ed S M Kuebler and V T Milam vol 1179E (Cambridge: Cambridge University Press) pp 1179–BB08–02
- [34] Peralta-Martinez M V and Wakeham W A 2001 Thermal conductivity of liquid tin and indium *Int. J. Thermophys.* **2** 395–403
- [35] Huber M, Harvey A, Horton H, Ryffel H and McCauley C 2011 Thermal conductivity of gases *CRC Handbook of Chemistry and Physics* 92nd edn (Boca Raton, FL: CRC Press) pp 6–2240
- [36] Fiedler K R, McLeod E and Troian S M 2018 Differential colorimetry measurements of fluctuation growth in nanofilms exposed to large thermal gradients arXiv:1808.04693
- [37] Fiedler K R and Troian S M 2016 Early time instability in nanofilms exposed to a large transverse thermal gradient: improved image and thermal analysis *J. Appl. Phys.* **120** 205303
- [38] McLeod E, Liu Y and Troian S M 2011 Experimental verification of the formation mechanism for pillar arrays in nanofilms subject to large thermal gradients *Phys. Rev. Lett.* **106** 175501

- [39] Cross M and Greenside H 2009 *Pattern Formation and Dynamics in Nonequilibrium Systems* (Cambridge: Cambridge University Press)
- [40] Mitlin V S 1993 Dewetting of solid surface: analogy with spinodal decomposition *J. Colloid Interface Sci.* **156** 491–7
- [41] Giacomelli L and Otto F 2003 Rigorous lubrication approximation *Interfaces Free Bound.* **5** 483–529
- [42] Laugesen R S and Pugh M C 2002 Energy levels of steady states for thin-film-type equations *J. Differ. Equ.* **182** 377–415
- [43] Krechetnikov R 2010 On application of lubrication approximations to nonunidirectional coating flows with clean and surfactant interfaces *Phys. Fluids* **22** 092102
- [44] COMSOL Inc. Multiphysics V5.3 (Burlington, MA)
- [45] Witelski T P and Bernoff A J 1999 Stability of self-similar solutions for van der Waals driven thin film rupture *Phys. Fluids* **11** 2443–5
- [46] Grigoriev R O and Qin T 2018 The effect of phase change on stability of convective flow in a layer of volatile liquid driven by a horizontal temperature gradient *J. Fluid Mech.* **838** 248–83
- [47] Garnier N, Grigoriev R O and Schatz M F 2003 Optical manipulation of microscale fluid flow *Phys. Rev. Lett.* **91** 054501